New Journal of Physics

The open access journal at the forefront of physics

PAPER

CrossMark

Isotope shifts in cadmium as a sensitive probe for physics beyond the standard model

B Ohayon[1,*] , S Hofsäss[2] , J E Padilla-Castillo[2], S C Wright[2], G Meijer[2], S Truppe[2,5,*] , K Gibble[3,*] and B K Sahoo[4,*]

1 Institute for Particle Physics and Astrophysics, ETH Zürich, CH-8093 Zürich, Switzerland
2 Fritz-Haber-Institut der Max-Planck-Gesellschaft, Faradayweg 4-6, 14195 Berlin, Germany
3 Department of Physics, Pennsylvania State University University Park, State College, PA 16802, United States of America
4 Atomic and Molecular Physics Division, Physical Research Laboratory, Navrangpura, Ahmedabad 380009, India
5 Current address: Centre for Cold Matter, Blackett Laboratory, Imperial College London, Prince Consort Road, London SW7 2AZ, United Kingdom
* Authors to whom any correspondence should be addressed.

E-mail: bohayon@ethz.ch, truppe@fhi-berlin.mpg.de, kgibble@psu.edu and bijaya@prl.res.in

Abstract

Isotope shifts (ISs) of atomic energy levels are sensitive probes of nuclear structure and new physics beyond the standard model. We present an analysis of the ISs of the cadmium atom (Cd I) and singly charged cadmium ion (Cd II). ISs of the 229 nm, 326 nm, 361 nm and 480 nm lines of Cd I are measured with a variety of techniques; buffer–gas-cooled beam spectroscopy, capturing atoms in a magneto-optic-trap, and optical pumping. IS constants for the D_1 and D_2 lines of Cd II are calculated with high accuracy by employing analytical response relativistic coupled-cluster theory in the singles, doubles and triples approximations. Combining the calculations for Cd II with experiments, we infer IS constants for all low-lying transitions in Cd I. We benchmark existing calculations via different many-body methods against these constants. Our calculations for Cd II enable nuclear charge radii of Cd isotopes to be extracted with unprecedented accuracy. The combination of our precise calculations and measurements shows that King plots for Cd I can improve the state-of-the-art sensitivity to a new heavy boson by up to two orders of magnitude.

1. Introduction

The most accurately determined quantities are transition frequencies of optical clocks [1], which are measured to better than 10^{-18}. This superb spectroscopic precision enables stringent searches for new physics [2–5]. One approach compares the isotope shifts (ISs) of two or more transitions as in a King plot (KP) [6], in which a deviation from a linear behaviour [7–10] can be a signature for beyond standard model (BSM) physics, such as a new boson mediating a force between electrons and neutrons. KP searches are applicable to systems possessing narrow optical transitions for which ISs can be measured with high precision, even with extraordinary sub-Hz accuracy using common-mode noise rejection [11, 12]. Searches for deviations from linearity with KPs require a minimum of four stable (or long-lived) even–even isotopes, which severely restricts the number of candidate elements.

BSM searches through KP non-linearity were performed for two elements in different regimes. On the low atomic number (Z) side are measurements in calcium ($Z = 20$); the lightest element with more than three stable even–even isotopes. A KP comprised of two transitions with different relativistic effects for Ca II, with a characteristic precision of 20 Hz, shows no non-linearity, translating directly to limits on several BSM scenarios [13]. As experimental precision improves, the potential for new physics searches using KPs in light elements such as Ca is expected to be limited by the difficulty of calculating the standard model (SM) contribution to the KP non-linearity resulting from high-order recoil effects in a light many-electron system [14, 15].
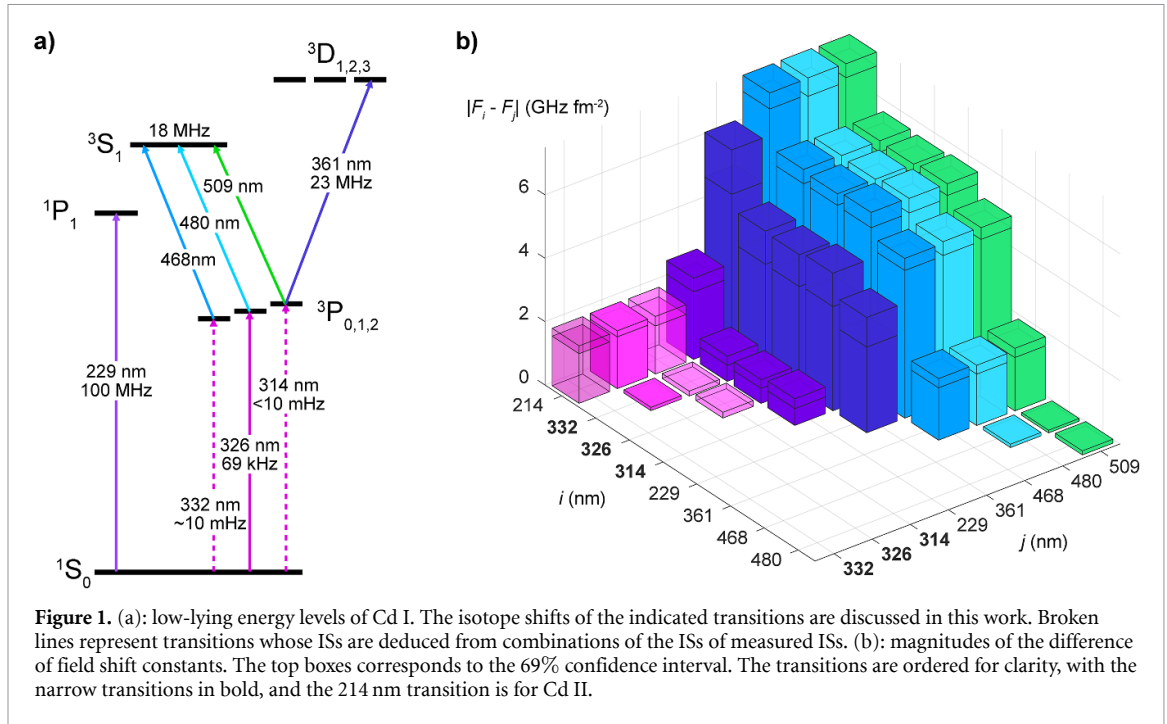
Figure 1. (a): low-lying energy levels of Cd I. The isotope shifts of the indicated transitions are discussed in this work. Broken lines represent transitions whose ISs are deduced from combinations of the ISs of measured ISs. (b): magnitudes of the difference of field shift constants. The top boxes corresponds to the 69% confidence interval. The transitions are ordered for clarity, with the narrow transitions in bold, and the 214 nm transition is for Cd II.

In the high Z regime, the effects of a new massive boson are more pronounced [7, 15], while recoil effects are heavily suppressed. However, other sources of SM non-linearity become dominant making the interpretation of an observed non-linearity more involved. For Yb ($Z = 70$), ISs in several ionic and atomic lines were measured with high-precision [16–19]. A recent analysis encompassing all of the experimental data indicates a strong non-linearity attributed to nuclear deformation [19], which currently cannot be calculated *ab initio* with sufficient precision. This behaviour is particularly pronounced and follows from Yb isotopes being amongst the most deformed in the stable region of the nuclear chart [20]. A non-linearity from an additional source was identified, whose origin is currently being studied [17, 19]. Considering the cases above, once a non-linearity is observed, it is not straightforward to interpret it as a signature of new physics. Pronounced non-linearities in several systems will add clarity. Moreover, there is a trade-off between lower values of Z, where both the non-linearities arising from the SM and those that come from new physics effects are less pronounced; and higher values of Z, where several sources of non-linearity may be difficult to disentangle due theoretical intractability.

Cadmium ($Z = 48$) sits in between these two limits. Having a relatively simple atomic structure and narrow transitions [21, 22], it is a prime candidate for new physics searches via KP non-linearities. Being close to the $Z = 50$ proton shell closure makes Cd nuclei much less deformed than e.g. Yb, suppressing a major source of SM non-linearity. Cd possesses six stable even–even isotopes, which could allow up to three different sources of non-linearity to be identified. In this work, we present measurements of ISs in the neutral cadmium atom (Cd I). We combine these measurements with literature values and highly accurate calculations of IS constants for transitions in the singly charged cadmium ion (Cd II). This enables us to map out all of the IS constants of the low-lying transitions in Cd I shown in figure 1, and identify the promising combinations for BSM searches. We compare the obtained IS constants with recent calculations and discuss the current state of the art in calculating these constants for two-valence systems. Such calculations are needed to assess the sensitivity of KPs to specific new physics models. We also combine calculated IS constants with measurements in a long chain of short-lived isotopes to yield highly accurate charge radii differences, which are needed to determine the nuclear contributions to KP non-linearities [17, 23]. Finally, we discuss the prospects for searches for BSM physics via KPs in Cd in light of our analysis.

2. Theory

The IS $\delta\nu_i^{A,A'}$ between isotopes with mass numbers A, A', at the precision of the measurements analysed here, can be written as [24]

$$\delta\nu_i^{A,A'} = F_i \delta\lambda^{A,A'} + K_i \mu^{A,A'}. \tag{1}$$

Here $\mu^{A,A'} = 1/M_A - 1/M_{A'}$ the inverse nuclear mass difference, i denotes a particular atomic transition, and $\delta\lambda^{A,A'} = \Sigma_k S_{2k}(\delta r_c^{2k})^{A,A'}$ is the nuclear parameter [25], which is expanded in a series of even charge moments

$$r_c^k = \frac{\int r^k \rho(r) r^2 \, dr}{\int \rho(r) r^2 \, dr}. \tag{2}$$

For brevity, we denote the root mean square (RMS) charge radius $\sqrt{r_c^2}$ here as r_c. The constants F_i and K_i are the field shift and mass shift, which depend only on the transition in question at this level. To calculate these constants, the nuclear charge distribution can be approximated using a Fermi distribution

$$\rho(r) = \frac{\rho_0}{1 + e^{(r-b)/a}}, \tag{3}$$

where ρ_0 is a normalization constant, and b and a are determined from electron scattering experiments [26, 27].

The operator for the field shift is given by

$$F = -\sum_e \frac{\delta V_{\text{nuc}}(r_c, r_e)}{\delta\lambda} \approx -\sum_e \frac{\delta V_{\text{nuc}}(r_c, r_e)}{\delta\langle r_c^2 \rangle}(1 + f_\lambda) \tag{4}$$

where the electrostatic potential V_{nuc} is a function of r_c, the radial distance of an electron is r_e, and the sum is over all electrons of the system. The contribution from higher nuclear moments f_λ is estimated as

$$f_\lambda \approx -S_4 \frac{r_c^4}{r_c^2} - S_6 \frac{r_c^6}{r_c^2} = 2.8(3)\%, \tag{5}$$

where the Seltzer coefficients S_4 and S_6 are estimated for the $5S$ levels of Cd II [25], and the ratio of moments is taken from two parameterizations of electron scattering experiments [26, 27]. The uncertainty of f_λ is estimated from the model-dependence of the charge distribution of equation (3), and its variation between isotopes.

The mass shift constant can further be split into a normal mass shift (NMS) and specific mass shift (SMS). The operators to determine the NMS and SMS constants are defined in a relativistic framework as [28, 29]

$$K^{\text{NMS}} = \frac{1}{2}\sum_i \left(\vec{p}_i^{\,2} - \frac{\alpha Z}{r_i}\vec{\alpha}_i^D \cdot \vec{p}_i - \frac{\alpha Z}{r_i}(\vec{\alpha}_i^D \cdot \vec{C}_i^1)\vec{C}_i^1 \cdot \vec{p}_i \right) \tag{6}$$

and

$$K^{\text{SMS}} = \frac{1}{2}\sum_{i\neq j} \left(\vec{p}_i \cdot \vec{p}_j - \frac{\alpha Z}{r_i}\vec{\alpha}_i^D \cdot \vec{p}_j - \frac{\alpha Z}{r_i}(\vec{\alpha}_i^D \cdot \vec{C}_i^1)(\vec{p}_j \cdot \vec{C}_j^1) \right), \tag{7}$$

where the p_i's are the components of the momentum operator, α^D is the Dirac matrix, and C^1 is the Racah operator. We note that there are slight modifications in the definitions of the F, K^{NMS} and K^{SMS} operators if we include quantum electrodynamics (QED) interactions. These contributions are expected to be smaller than our reported uncertainties.

A linear relation results after applying equation (1) to the measured ISs of two transitions (i, j):

$$\delta\bar{\nu}_i^{A,A'} = F_{ij}\delta\bar{\nu}_j^{A,A'} + K_{ij} \tag{8}$$

with the modified ISs $\delta\bar{\nu}_i^{A,A'} = \delta\nu_i^{A,A'}/\mu^{A,A'}$, the slope $F_{ij} = F_i/F_j$, and the offset $K_{ij} = K_i - F_{ij}K_j$. In this work we find that the linear relation of equation (8) holds at the $\sim$ MHz-level for all Cd transition pairs. It may therefore be used to project IS constants from one transition to another. We calculate IS constants for transitions in Cd II using the analytical response (AR) relativistic coupled-cluster (RCC) method, and project them using equation (8) to atomic transitions.

3. The AR-RCC method

We begin with the Dirac–Coulomb (DC) Hamiltonian:

$$H_{\text{DC}} = \sum_i \left[c\vec{\alpha}_i^D \cdot \vec{p}_i + (\beta_i - 1)c^2 + V_{\text{nuc}}(r_i) \right] + \sum_{i,j>i} \frac{1}{r_{ij}}, \tag{9}$$

where c is the speed of light, $\vec{\alpha}^D$ and β are the Dirac matrices, $\vec{p}$ is the single particle momentum operator. $\sum_{i,j} \frac{1}{r_{ij}}$ represents the Coulomb potential between the electrons located at the ith and jth positions. Corrections from the Breit and QED interactions are estimated by adding the corresponding potential terms as in [30], yielding the atomic Hamiltonian H_0.

We consider the nuclear charge distribution of equation (3) to define the potential V_{nuc} [31]

$$V_{\text{nuc}}(r) = -\frac{Z}{\mathcal{N}r} \begin{cases} \frac{1}{b}\left(\frac{3}{2} + \frac{a^2\pi^2}{2b^2} - \frac{r^2}{2b^2} + \frac{3a^2}{b^2}P_2^+ \frac{6a^3}{b^2 r}(S_3 - P_3^+) \right) & \text{for } r_i \leqslant b \\ \frac{1}{r_i}\left(1 + \frac{a62\pi^2}{b^2} - \frac{3a^2 r}{b^3}P_2^- + \frac{6a^3}{b^3}(S_3 - P_3^-) \right) & \text{for } r_i > b, \end{cases} \tag{10}$$

with

$$\mathcal{N} = 1 + \frac{a^2\pi^2}{b^2} + \frac{6a^3}{b^3}S_3, \; S_k = \sum_{l=1}^{\infty} \frac{(-1)^{l-1}}{l^k}e^{-lb/a}, \; P_k^{\pm} = \sum_{l=1}^{\infty} \frac{(-1)^{l-1}}{l^k}e^{\pm l(r-b)/a}. \tag{11}$$

We determine these constants for the ground state, $[4d^{10}]5s$, and the first two excited states, $[4d^{10}]5p_{1/2}$ and $[4d^{10}]5p_{3/2}$ of Cd II to study the ISs of its D_1 and D_2 lines.

In the RCC theory ansatz, the wave function of the above atomic states are constructed as [32–34]

$$|\Psi_v\rangle = e^T\{1 + S_v\}|\Phi_v\rangle, \tag{12}$$

where $|\Phi_v\rangle$ is a mean-field wave function from a Dirac-Hartree–Fock (DHF) treatment, and T and S_v are the excitation operators that account for electron correlations from the core orbitals and valence orbital, respectively. The subscript v denotes the valence orbital associated with the respective state. It is introduced to uniquely identify the states having the common closed-shell configuration $[4d^{10}]$. Considering the IS operators, F, K^{NMS} and K^{SMS}, denoted as O in the total Hamiltonian as $H = H_0 + \eta O$, we express the above wave function in the AR-RCC formulation as

$$|\Psi_v\rangle = |\Psi_v^{(0)}\rangle + \eta|\Psi_v^{(1)}\rangle + \mathcal{O}(\eta^2), \tag{13}$$

with an energy

$$E_v = E_v^{(0)} + \eta E_v^{(1)} + \mathcal{O}(\eta^2). \tag{14}$$

Here η is nominally equal to one and is introduced for the perturbation expansion in orders of O, denoted by the superscripts. $E_v^{(0)}$ corresponds to the contribution from H_0 and $E_v^{(1)}$ includes first-order contributions from O and electron correlations. The above can be implemented in the RCC theory by expanding the RCC operators as

$$T = T^{(0)} + \eta T^{(1)} + \mathcal{O}(\eta^2) \tag{15}$$

and

$$S_v = S_v^{(0)} + \eta S_v^{(1)} + \mathcal{O}(\eta^2). \tag{16}$$

The $\mathcal{O}(\eta^2)$ contributions are usually small and neglected in IS calculations. However, these non-linear contributions can be significant when probing BSM physics. The zeroth-order RCC operator amplitudes follow from

$$\langle \Phi_0^*|\bar{H}_0|\Phi_0\rangle = 0 \tag{17}$$

and

$$\langle \Phi_v^*|\{(\bar{H}_0 - E_v^{(0)})S_v^{(0)}\} + \bar{H}_0|\Phi_v\rangle = 0, \tag{18}$$

where $\langle \Phi_{0,\nu}^* |$ denotes for all possible excited Slater determinants and $\bar{H}_0 = \left(H_0 e^{T^{(0)}} \right)_{\text{conn}}$, where the subscript conn denotes for only connected terms in the expansion. With these amplitudes of the RCC operators, we calculate the zeroth-order energies as

$$E_0^{(0)} = \langle \Phi_0 | \bar{H}_0 | \Phi_0 \rangle \tag{19}$$

and

$$E_\nu^{(0)} = \langle \Phi_\nu | \bar{H}_0 \{ 1 + S_\nu^{(0)} \} | \Phi_\nu \rangle, \tag{20}$$

where $E_0^{(0)}$ is the energy of the common closed-core of the considered atomic states, $[4d^{10}]$ for Cd II. In the actual calculations, we consider a normal-ordered Hamiltonian defined with respect to $[4d^{10}]$. Therefore, $E_\nu^{(0)}$ corresponds to the electron affinity, $E_\nu^{(0)} - E_0^{(0)}$, of the valence orbital relative to the $[4d^{10}]$ configuration. We note that equations (18) and (20) are coupled.

In the AR-RCC theory, we calculate the desired FS, NMS and SMS constants as the first-order energy corrections $E_\nu^{(1)} \equiv \langle \Psi_\nu^{(0)} | O | \Psi_\nu^{(0)} \rangle$ using the following expression [30, 35]

$$E_\nu^{(1)} = \langle \Phi_\nu | \overline{H_0} S_\nu^{(1)} + (\overline{H_0} T^{(1)} + \overline{O}) \{ 1 + S_\nu^{(0)} \} | \Phi_\nu \rangle, \tag{21}$$

where $\overline{O} = (O e^{T^{(0)}})_{\text{conn}}$. Here, the normal-ordered form of operators again yield calculated values relative to the contributions from the $[4d^{10}]$ configuration. The amplitudes of the first-order perturbed RCC operators are given by

$$\langle \Phi_0^* | \overline{H}_0 T^{(1)} + \overline{O} | \Phi_0 \rangle = 0. \tag{22}$$

and

$$\langle \Phi_\nu^* | (\overline{H}_0 - E_\nu^{(0)}) S_\nu^{(1)} + \left(\overline{H}_0 T^{(1)} + \overline{O} \right) \{ 1 + S_\nu^{(0)} \} | \Phi_\nu \rangle = 0. \tag{23}$$

We use Gaussian type orbitals (GTOs) [36] to construct the single particle DHF wave functions. The large and small radial components of the DHF orbitals, $P(r)$ and $Q(r)$, are expressed using these GTOs as

$$P(r) = \sum_{k=1}^{N_k} c_k^{\mathcal{L}} \zeta_{\mathcal{L}} r^l e^{-\eta_0 \gamma^k r^2} \tag{24}$$

and

$$Q(r) = \sum_{k=1}^{N_k} c_k^{\mathcal{S}} \zeta_{\mathcal{L}} \zeta_{\mathcal{S}} \left(\frac{d}{dr} + \frac{\kappa}{r} \right) r^l e^{-\eta_0 \gamma^k r^2}, \tag{25}$$

where l is the orbital quantum number, κ is the relativistic angular momentum quantum number, $c_k^{\mathcal{L}(\mathcal{S})}$ are the expansion coefficients, $\zeta_{\mathcal{L}(\mathcal{S})}$ are the normalization factors of GTOs, η_0 and γ are optimized GTO parameters for a given orbital, and N_k represents the number of GTOs. To construct the GTOs, we use $\eta_0 = 0.00715, 0.0057, 0.0072, 0.0052$ and 0.0072 for s, p, d, f and g orbitals, respectively, with corresponding γ values $1.92, 2.04, 1.97, 2.07$ and 2.54. Since our orbitals are not bounded, we integrate to an upper radial limit of $r = 500$ a.u. on a grid using a 10-point Newton–Cotes Gaussian quadrature method. Our numerical calculations use exponential grids with a step-size of 0.016 a.u. and 1200 grid points, and the coefficients are determined by the Roothan equation in the relativistic framework. To reduce the required computational resources, we have limited the virtual space by considering all possible single and double excitations in the AR-RCC theory (AR-RCCSD method) for the $1-20s, 2-20p, 3-20d, 4-17f$, and $5-14g$ orbitals. The AR-RCCSDT method adds triple excitations to the above single and double excitations only for the $16s, 16p, 14d, 10f$, and $5g$ orbitals.

Table 1. Cd II Energies and IS constants for the ground and first two excited states, and their transitions for the D_1 (226.5 nm) and D_2 (214.4 nm) lines.

(a) Electron affinities and transition energies (cm^{-1})				
Method	E_{5S}	$E_{5P1/2}$	$E_{5P3/2}$	E_{D1}	E_{D2}
DHF	124 568	84 903	82 871	39 666	41 698
RCCSD	13 6013	91 858	89 357	44 155	46 657
RCCSDT	136 717	92 401	98 974	44 316	46 843
$+\Delta$Breit	−83	−83	−50	0.	−33
$+\Delta$QED	−100	−4	−6	−97	−94
SUM	136 533(200)	92 314(150)	89 818(150)	44 218(97)	46 715(104)
Exp [37, 38]	136 374.7(1)	92 238.7(1)	89 756.2(1)	44 136.1(1)	46 618.6(1)

(b) Normal mass shift (GHz u)				
Method	$K_{NMS,5S}$	$K_{NMS,5P1/2}$	$K_{NMS,5P3/2}$	$K_{NMS,D1}$	$K_{NMS,D2}$
DHF	5952	3374	3163	2578	2789
AR-RCCSD	2113	1381	1339	732	774
AR-RCCSDT	2204(20)	1470(15)	1426(15)	734(7)	778(8)
$+\Delta$Breit	−4	−4	−2	0.	−2
$+\Delta$QED	−7(2)	0.	0.	−7(2)	−7(2)
SUM	2194(20)	1466(15)	1424(15)	727(8)	769(8)
Scaling	2243	1517	1476	726	767

(c) Specific mass shift (GHz u)				
Method	$K_{SMS,5S}$	$K_{SMS,5P1/2}$	$K_{SMS,5P3/2}$	$K_{SMS,D1}$	$K_{SMS,D2}$
DHF	−2775	−1753	−1488	−1022	−1287
AR-RCCSD	1288	123	256	1165	1032
AR-RCCSDT	1343(15)	129(5)	260(7)	1214(16)	1083(17)
$+\Delta$Breit	12	5	4	7	8
$+\Delta$QED	4(1)	−2(0.)	−2(0.)	6(1)	5(1)
SUM	1359(15)	132(5)	263(7)	1226(16)	1096(17)

(d) Total mass shift (GHz u)				
Method	K_{5S}	$K_{5P1/2}$	$K_{5P3/2}$	K_{D1}	K_{D2}
$K_{SMS}+K_{NMS}$	3552(25)	1598(16)	1686(17)	1954(18)	1866(19)
CI-MBPT [39]				1770(300)	1667(300)
CKP [39]					2199(507)

(e) Field shift (MHz fm^{-2})				
Method	F_{5S}	$F_{5P1/2}$	$F_{5P3/2}$	F_{D1}	F_{D2}
DHF	−4778	−59	−0.	−4719	−4778
AR-RCCSD	−6140	−177	−100	−5963	−6040
AR-RCCSDT	−6227(20)	−232(5)	−152(5)	−5995(21)	−6075(21)
$+\Delta$Breit	22	1	1	21	21
$+\Delta$QED	147(37)	4(1)	3(1)	143(36)	144(36)
$-f_\lambda$	−172(17)	0	0	−172(17)	−172(17)
SUM	−6230(45)	−277(5)	−149(5)	−6003(45)	−6082(45)
CI-MBPT [39]				−6067(300)	−6144(300)
CKP [39]					−6621(530)

4. Calculated IS constants for Cd II

An important test of *ab initio* methods to obtain accurate atomic wave functions is to compare the calculated energies with the measured ones. In table 1(a) we present the calculated electron affinities of the ground and first two excited states of Cd II. From these values, we determined the excitation energies of the D_1 and D_2 transitions given in table 1(a). The RCCSDT results show that triple excitations contribute more to the electron affinities than to the excitations energies, and that the Breit and QED corrections are significant. The uncertainties of the calculated energies are estimated from the convergence. We reproduce the experimental

transition energies to 0.2%, an order of magnitude of improvement over CI-MBPT calculations for these transitions [39]. The high accuracy with which experimental energies are reproduced using the RCC method validates the accuracy of our wave functions for the following IS constants calculation. However, accurate wavefunctions are a necessary but insufficient condition for obtaining accurate IS constants. Various many-body methods for calculating the operators produce significantly different results for the IS constants; the AR method performs well against stringent benchmarks [30, 40].

We present IS constants using the DHF, AR-RCCSD and AR-RCCSDT methods in table 1. Uncertainties from H_{DC} and Breit interactions to the AR-RCCSDT results are estimated by determining contributions from the h, i and j higher angular momentum orbitals, as well as quadruple excitations from the s, p and d lower angular momentum orbitals through a perturbative analyses by using amplitudes of the valence correlation operators $S_v^{(0)}$ and $S_v^{(1)}$. These comes out to be 10%–20% of the different properties compared to the contributions from the triples effects alone (differences between the RCCSD and RCCSDT results). Since the QED effects are estimated using a model potential and neglecting their effects in the definitions of the IS operators, higher uncertainties (25% compared with their total values) are assigned.

Focusing first on the NMS constants, they can be obtained in the nonrelativistic limit by invoking the Virial theorem [41]. This results in the scaling law $K_{NMS} \approx E \cdot m_e$, where E is the experimental energy and m_e the electron mass in atomic units. However, for a medium mass system such as Cd II, it is not *a priori* clear how applicable this method is. Table 1(b) gives our results for K_{NMS} calculated using the corresponding relativistic operator in equation (6). We see that for the D_1 and D_2 transitions, the scaling law agrees with our calculation within the 1% numerical accuracy. This behaviour is attributed to strong cancellations of relativistic contributions to the NMS in transitions with the same principal quantum number [42]. For the ground state the scaling law is accurate to 2%–3%. Triple excitations contribute significantly to the NMS constants for the electron affinities, even though these quantities are evaluated with a one-body operator. We thus expect that for similar transitions in lighter systems, for which the contribution of electron correlations to the NMS is more pronounced, using the scaling-law could be preferable to a fully relativistic calculation.

The SMS is associated with the two-body operator of equation (7) and thus strongly affected by high-order electron correlations, which are challenging to estimate [43]. Even in modern calculations, an uncertainty of 10%–20% in K_{SMS} is usually given (see e.g. [35, 39, 44–46]). Our results in table 1(c) are quoted with an a accuracy of 1%–2%, attributed to higher-order electron correlations, which we estimate perturbatively. This is in contrast to K_{NMS} and the energies, whose uncertainties follow from numerical convergence. We see that the sign of K_{SMS} changes between the DHF and AR-RCCSD calculations. This points to the importance of strong electron correlations in K_{SMS}, with a 10% difference coming from triple excitations. Owing to the two-body nature of the SMS operator, triple excitations in the AR-RCC method take several months to calculate at a typical high-performance computing facility. The total mass shift constant $K = K_{NMS} + K_{SMS}$ in table 1(d) agrees well with, and is an order of magnitude more precise than, a recent CI-MBPT calculation for both ionic transitions [39], as well as a calibrated King plot (CKP) estimation combining muonic x-ray and electron scattering measurements with precise ISs for the D_2 transition [39]. The contributions of the Breit and QED interaction to K are found to be negligible at the current level of precision.

The calculation of the field shift operator is considered robust for a number of systems. Various methods typically agree at the few percent level [16, 30, 40, 47–52]. In Cd II, F convergences quickly, with triple excitations contributing only 0.6%. This yields an 0.35% uncertainty of F at the AR-RCCSDT level, which could be reduced further with more computational resources. However, we find that QED effects, which are often not taken into account in such calculations, are not negligible. In fact, our final uncertainty for F is dominated by the systematic uncertainty associated with QED correction only being present at the Hamiltonian level. This is expected to be even more pronounced in heavier systems such as Yb, where calculations of F are given with sub-percent numerical precision [53]. Our results in table 1(e) agree with the CI-MBPT and a CKP results of [39]. To our knowledge, this is the first calculation of F with sub-percent accuracy (computational and systematic) for a system with more than 19 electrons.

5. IS measurements in the Cd atom

In this section we describe our IS measurements of four transitions of Cd I for all stable bosonic isotopes. Measurements are done with two experimental systems employing different frequency calibration procedures. A more detailed description of the experimental systems, as well as results for the fermionic isotopes and absolute wavenumbers, will be given in upcoming publications [54]. Our results are given in table 2, along with available previous measurements, which disagree significantly in several cases. The two independent experimental results at 326 nm agree to within 0.5–1.6 combined standard errors, whereas the disagreements with these previous measurements are as large as four combined errors.

Table 2. Isotope shifts of Cd I in MHz, relative to ^{114}Cd. Derived values are in italics; for the 332 nm clock line, from this work and previous measurements of 468 nm ISs [55], and similarly for the narrow 314 nm transition using 509 nm ISs [56].

A	229 nm	326 nm	480 nm	361 nm	332 nm	314 nm
106	1818.1(3.5)[a]	1911.2(3.3)[a]	−798.5(1.0)[c]	−607.6(3.0)[b]	1911.4(4.7)	1915.5(3.9)
	1748(11) [57]	1913.0(1.0)[b]				
		1921(26) [58, 59]				
108	1336.5(3.4)[a]	1399.4(3.3)[a]	−586.7(1.0)[c]	−447.4(3.0)[b]	1404.5(3.7)	1403.9(3.0)
	1258(9) [57]	1402.4(1.0)[b]				
		1410(40) [59]				
110	865.0(3.3)[a]	909.3(3.3)[a]	−383.4(1.0)[c]	−293.9(1.0)[b]	914.1(2.1)	913.7(2.1)
	826(6) [57]	914.7(1.0)[b]				
	906(35) [60]	*909(13)* [58, 61, 62]				
112	407.5(3.3)[a]	426.3(3.3)[a]	−183.1(1.0)[c]	−142.2(1.0)[b]	428.9(1.7)	429.7(1.6)
	392(5) [57]	429.9(1.0)[b]				
	396(30) [60]	*403(11)* [58, 61, 62]				
116	−316.1(3.3)[a]	−326.9(3.3)[a]	152.7(1.0)[c]	122.0(1.0)[b]	−320.6(1.7)	−320.2(1.7)
	−299(4) [57]	−321.5(1.0)[b]				
		−279(12) [58, 62]				

[a] Beam measurement.

[b] Blue MOT edge.

[c] MOT optical pumping rate.

5.1. Atomic beam measurements of 229 and 326 nm ISs

We carried out laser induced fluorescence spectroscopy with a buffer–gas-cooled beam. A pulsed beam is produced by laser ablation of a Cd target, which is mounted in a buffer–gas cell. Cryogenic helium gas (3 K) flows continuously through the cell, cools the hot atoms and extracts them into an atomic beam with a mean forward velocity of roughly 120 m s^{-1}. The laser light intersects the atomic beam perpendicularly, and fluorescence is collected on a UV-sensitive photomultiplier tube. The transverse velocity of the atoms is reduced to below about 0.5 m s^{-1} by a slit directly before they enter the fluorescence detector. The resulting Doppler broadenings are 1.5 MHz (326 nm) and 2.1 MHz (229 nm).

Due to the large natural linewidth of the 229 nm line, $\Gamma/(2\pi) = 100(3)$ MHz [54], a high-precision IS measurement is hampered by the overlap of the different isotopes in the spectrum. To improve the accuracy, we use enriched targets to precisely determine the lineshape. A Lorentzian function fits the data well, suggesting that Doppler broadening is indeed negligible. We then measure the IS of the (110, 112) pair, for which the overlap in the spectrum is most severe. This is done by taking multiple spectra while alternating two separate enriched ablation targets for ^{110}Cd and ^{112}Cd. This IS is then fixed in a fit to the spectrum recorded using an ablation target with natural abundance. To resolve the frequencies of the fermionic isotopes in the spectrum, we vary their amplitude relative to the bosonic isotopes by changing the polarisation angle of the excitation laser with respect to the detector axis. The weighted means for each isotope are averaged and the final result is given in table 2 and plotted in figure 3(a). Our results are more accurate and differ considerably from those of a recent measurement [57]. This discrepancy manifests itself as a horizontal offset in the fits to the experimental data portrayed in figure 3(a).

The 326 nm intercombination line of Cd has a 69 kHz natural linewidth that enables both cooling to low temperatures and precise spectroscopy. To measure the ISs of this line in an atomic beam, we use a frequency-doubled dye laser (Sirah Matisse 2DX with a Spectra Physics Wavetrain doubling module), whose linewidth is stabilised to better than 100 kHz short term and 1 MHz shot-to-shot stability. A typical spectrum is shown in figure 2, where the larger Doppler broadened linewidth of 5.6(2) MHz (Gaussian FWHM) arises from inclusion of atoms with higher velocity in the spectrum. The ISs of five independent measurements have an average standard deviation of 0.8 MHz, consistent with the wavemeter (HighFinesse WS8-10) resolution of 0.4 MHz at the fundamental wavelength. This statistical uncertainty is small compared with the systematic uncertainty in the wavemeter measurement of the laser frequency. To place an upper bound on this systematic uncertainty, we measure nearby optical transitions of atomic copper in the same beam machine. The D$_1$ (327.5 nm) and D$_2$ (324.8 nm) lines lie roughly 1.3 nm to either side of the 326 nm line in Cd. We reproduce the precisely measured ground state hyperfine intervals of ^{65}Cu (12 568.81(1) MHz) and ^{63}Cu (11 733.83(1) MHz) [65] with a mean deviation of 3.1 ± 2.0 MHz for ^{63}Cu and 1.8 ± 3.7 MHz for ^{65}Cu. By measuring the wavemeter linearity with a temperature and pressure stabilized Zerodur cavity we find a systematic uncertainty of 3.3 MHz. We assign this as our systematic frequency uncertainty for the 326 nm and 229 nm spectra of Cd I.
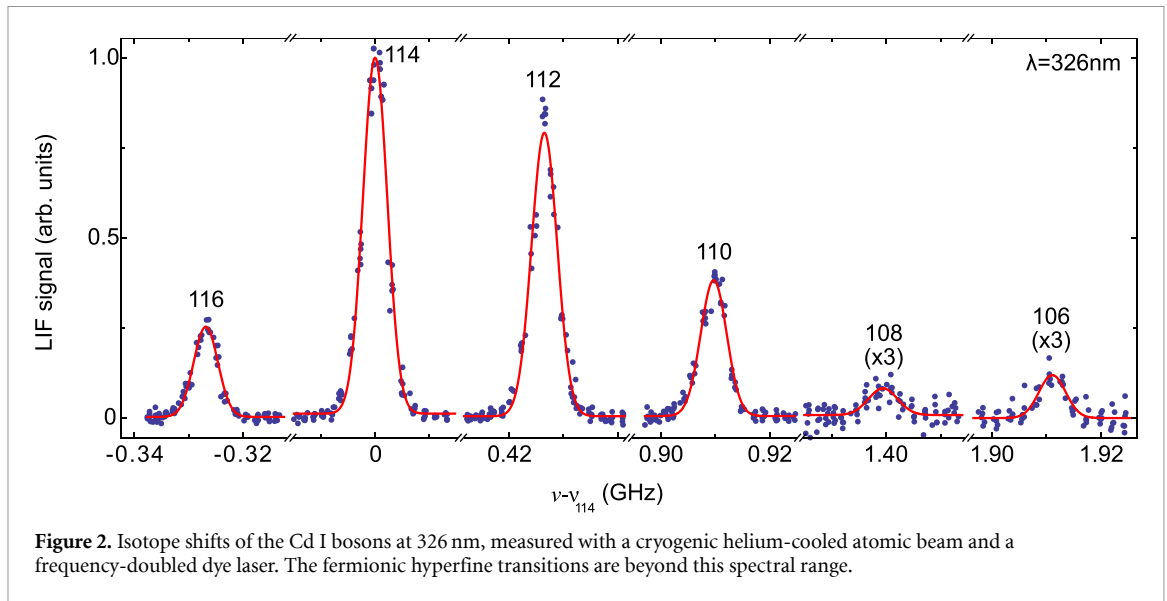
Figure 2. Isotope shifts of the Cd I bosons at 326 nm, measured with a cryogenic helium-cooled atomic beam and a frequency-doubled dye laser. The fermionic hyperfine transitions are beyond this spectral range.
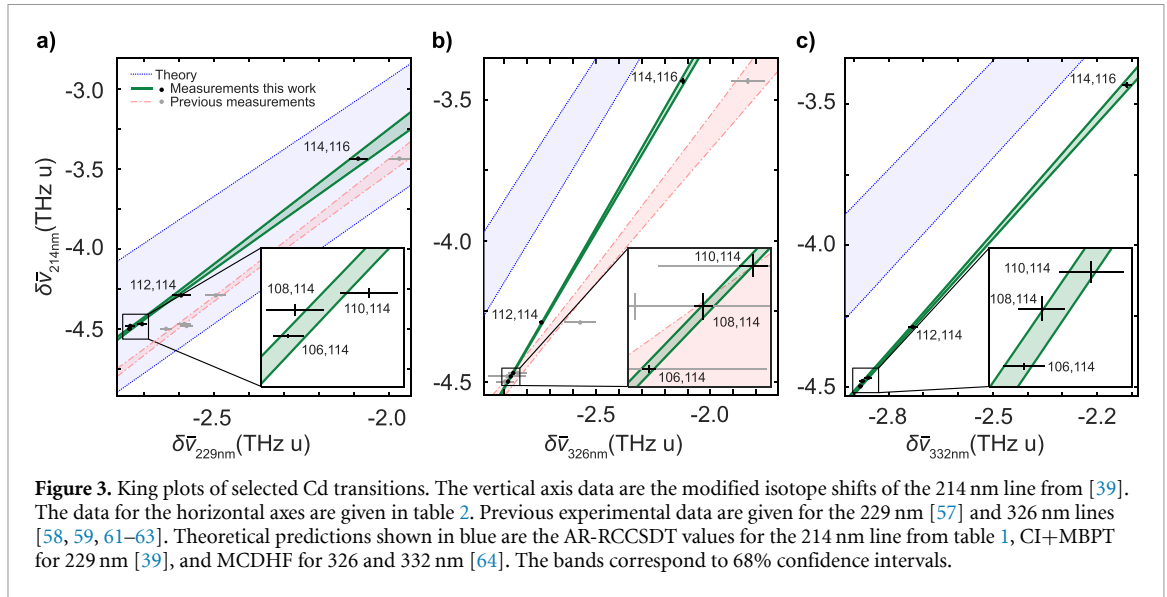
5.2. Measurements of 326, 480 and 361 nm ISs with magneto-optic traps

We also determine the ISs of the 326 line by measuring the sharp blue-edge of the fluorescence [66] from a 326 nm magneto-optic trap (MOT) []. The blue edge, where the cooling and trapping breaks down, is of order 20 kHz wide (90%–10%) and serves as a precise reference for ISs. We directly load a 326 nm MOT of the abundant isotopes, ^{110}Cd to ^{116}Cd, from an effusive 1.2 cm diameter source of natural Cd that is 2.2 cm from the MOT. To capture the atoms, we use 60 to 150 mW of 326 nm light that is frequency modulated with a peak-to peak amplitude of 8.6 MHz [22] and the three retro-reflected MOT beams have a diameter of 8.5 mm. A lower-intensity cooling stage follows the MOT loading, with no applied magnetic field gradient or frequency modulation, during which fluorescence is measured.

We produce 326 nm light with doubly-resonant sum frequency generation (SFG) of 542 and 820 nm light in a beta barium borate crystal [21]. The 542 nm light is produced by frequency doubling a fiber-amplified 1083 nm extended cavity diode laser (ECDL). An 820 nm ECDL and a tapered amplifier supply the 820 nm light. ISs are measured relative to various modes of a temperature-tuned, four-mirror, rectangular reference cavity. Its free-spectral range is 905.03 MHz, its tangential and sagittal transverse mode splittings are 201.04 MHz and 140.84 MHz, and the cavity linewidth is 350 kHz. The 1083 nm ECDL is locked to the 00, 01 and 10 cavity modes with an adjustable frequency offset provided by a double-passed acousto-optic modulator (AOM). The frequency of the 820 nm ECDL is measured relative to resonances of the same reference cavity [21], by slowly frequency modulating a double-passed AOM with a zero-to-peak amplitude of 1.2 MHz or less. Within 1 to 5 min after measuring the 326 nm frequency offset for each isotope, the absolute frequency of a 1083 nm cavity resonance is checked relative to a molecular iodine line via saturated absorption at 542 nm. We correct for the cavity drift between the measurements for each isotope, which is typically of order 1 MHz, and had a maximum drift of 4.2 MHz. The measurement uncertainty is given by the less than 1 MHz centering precision of the 820 nm light on a cavity resonance.

For ^{106}Cd and ^{108}Cd, with 1.25% and 0.89% natural abundances, we enhance the 326 nm MOT loading rate by capturing atoms on the 23 MHz wide 361 nm $^3P_2$-$^3D_3$ transition, after optical pumping from $^3P_1$ and $^3P_0$ to $^3P_2$ via the $^3S_1$ state (see figure 1(a)). The 361 nm light is generated via doubly-resonant SFG of 1083 nm and 542 nm light, producing 70 to 200 mW [21]. To load the 326 nm MOT, the 361 nm MOT is inhibited by turning off the 480 nm $^3P_1$—$^3S_1$ optical pumping light and allowing the atoms to equilibrate in the 326 nm MOT for 57 ms before the start of the 326 nm cooling and detection phase. Our results for the ISs for the 326 nm line are given in table 2 and figure 3(b). They are more accurate than our measurement of the same line with a beam, and comprise an order of magnitude of improvement compared with the weighted average of previous measurements. A disagreement of four combined errors is found for the (114 116) pair, previously measured with interferometry of fluorescence [58, 62]. This disagreement manifests as different slopes of the KP portrayed in figure 3(b).

To measure ISs for the 480 nm transition, we use all four laser sources to enhance the MOT loading and then inhibit the 480 nm light for 28 ms to transfer atoms to the 326 nm MOT and cool them. We then turn on a 4.4 ms low intensity pulse of 480 nm light and observe the resulting 361 nm fluorescence. We generate the 468 and 480 nm optical pumping light using single-pass SFG of 1083 nm light and 823 and 862 nm light in fiber-coupled PPLN waveguides. The 468 nm and 480 nm light are combined on a beamsplitter and the two

Figure 3. King plots of selected Cd transitions. The vertical axis data are the modified isotope shifts of the 214 nm line from [39]. The data for the horizontal axes are given in table 2. Previous experimental data are given for the 229 nm [57] and 326 nm lines [58, 59, 61–63]. Theoretical predictions shown in blue are the AR-RCCSDT values for the 214 nm line from table 1, CI+MBPT for 229 nm [39], and MCDHF for 326 and 332 nm [64]. The bands correspond to 68% confidence intervals.

output beams illuminate the atoms on three nearly orthogonal axes before being retro-reflected. The 862 nm laser, and thereby the frequency of the 480 nm light, is slowly stabilized with a wavemeter and is monitored with the same reference cavity, using a number of transverse modes and a zero-to-peak frequency modulation of 1.2 MHz via a double-passed AOM. We determine the center frequency of the 17.5 MHz wide transition with a resolution of 0.8 MHz using a slow square wave frequency modulation of the 480 nm light by ± 4 MHz with a double-passed AOM. Our 480 nm ISs in table 2 are the first measurements for this transition. By combining them with our 326 nm intercombination line ISs along with previous measurements for 468 nm [55], we determine the ISs for the 332 nm clock transition (see figure 3(c)), and similarly for the narrow 314 nm transition using measured 509 nm ISs [56].

Finally, we measure the ISs of the 361 nm $^3P_2$–$^3D_3$ transition. We again use the sharp blue-edge of the cooling as the reference for the ISs [66]. Here, we use the reference cavity stability to measure frequency offsets relative to 542 nm iodine saturated absorption resonances [67]. The blue edge is determined to better than 0.4 MHz and we estimate that the blue edges for the slower loading ^{106}Cd and ^{108}Cd MOTs may have systematic errors of order 3 MHz, much less than the 23 MHz 361 nm transition linewidth.

6. Benchmarking IS constants calculations

The constants of equation (8) for the D_1 and D_2 ionic transitions can be extracted from our calculation (table 1) with high accuracy because the uncertainties for each transition are highly correlated. We find $F_{D2,D1} = 1.0131(2)$ and $K_{D2,D1} = -114(2)$ GHz u. A Monte-Carlo fit to the available experimental data [56, 62, 68–70] yields $F_{D2,D1} = 1.02(6)$ and $K_{D2,D1} = -43(229)$ GHz u, which agrees with our calculation, within the large experimental uncertainty. To better test our calculation, recent ion-trap IS measurements for the D_2 transition [39] could be extended to the D_1 transition.

To test calculation in Cd I, we transform our constants for the Cd II D_2 transition to transitions in Cd I using equation (8), fitting experimental ISs from this work and the literature [39, 56–59, 62]. Here, we do not consider fermionic isotopes, for which equation (8) may not be a good approximation at the few MHz level [64]. The resulting IS constants are given in table 3. Their uncertainty is dominated by that of the measured ISs of the atomic lines. The IS constants of tables 1 and 3 agree with, and are up to an order of magnitude more precise than, the CI-MBPT calculations [39] for both F and K for all tested ionic and atomic transitions. We thus validate both the central values and the uncertainty estimation of CI-MBPT, which is applicable for calculations of both linear and non-linear IS constants in a variety of atomic systems.

For the intercombination line, our measurements produce a significantly larger KP slope than prior results, increasing from $F_{214,326} = 0.98(8)$ to $F_{214,326} = 1.397(17)$, corresponding to the green solid and red dashed lines in figure 3(b). Combining the slope with $F_{214} = -6082(45)$ MHz fm^{-2} from table 1(e) shifts F_{326} from $-6180(478)$ MHz fm^{-2} to $-4354(62)$ MHz fm^{-2}, closer to the value obtained for the 229 nm transition which is expected as they share an s-state. Our F_{326} and K_{326} constants agree with and are more accurate than CI-MBPT calculations [39] and an empirical CKP determination [71]. However, figure 3(b) shows a slight disagreement with a recent calculation via MCDHF [64]. As summarized in table 1(e), the deviation for F_{326} is two combined standard errors and for K_{326} by one. A similar deviation is apparent for

Table 3. IS constants of atomic transitions deduced from our calculations (table 1) projected using King plots with experimental data from table 2 and the literature [39, 56–59, 62].

i (nm)	F_i (MHz fm^{-2})	K_i (GHz u)	Method
229	−3764(134)	1199(104)	
	−4024(200)	1428(220)	CI-MBPT [39]
332	−4391(86)	1712(43)	
	−4660(160)	1629(19)	MCDHF [64]
326	−4354(62)	1673(43)	
	−4680(160)	1616(17)	MCDHF [64]
	−4559(230)	1865(400)	CI-MBPT [39]
	−4420(340)	1717(330)	CKP [71]
314	−4421(86)	1739(61)	
468	1150(49)	−1(47)	
480	1122(40)	30(41)	
509	1180(19)	−32(24)	
	1228(60)	−63(400)	CI-MBPT [39]
361	−654(42)	−237(59)	

the clock transition at 332 nm (figure 3(c)). The changes in F_{326} and K_{326} and the updated intercombination line ISs account for the 20%–50% differences between the ISs calculated in [64] and those summarized in [71]. Whereas the range of values of F_i is a few percent, we note that the many-body QED corrections are estimated to contribute 3%. Further improvements in field shift calculations should include these QED effects, especially for heavier elements.
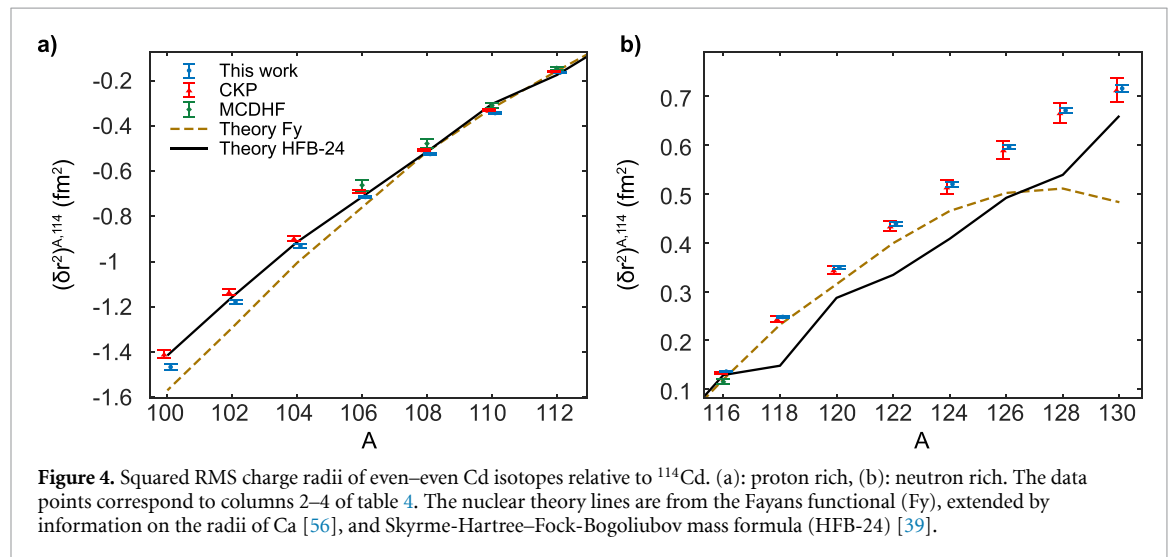
7. Improved charge radii

High-precision optical isotope and isomer shifts for the Cadmium chain were measured at ISOLDE using collinear laser spectroscopy [56, 72]. To extract charge radii differences from spectroscopic data, equation (1) is often calibrated with the radii of stable isotopes extracted from a combination of muonic x-ray energies and electron scattering data [71]. This commonly used CKP method has several disadvantages: it is currently applicable only to elements possessing at least three stable or long-lived isotopes; the determined IS constants are limited by the knowledge of nuclear polarization corrections to muonic levels, as well as their unknown correlations; the calibration coefficients from electron scattering experiments are in many cases unknown (e.g. for ^{106,108,111,113}Cd) or nuclear-model-dependent (e.g. for ^{110,112,114,116}Cd); and the resulting IS constants K and F are highly correlated, leading to diverging uncertainties of extracted radii outside of the calibrated region.

The advent of high-accuracy many-body calculations of IS constants allows differences of charge radii to be extracted directly from optical measurements with no input, beyond small higher-moment corrections, from muonic x-ray or electron scattering experiments. In table 4 and figure 4, we compare $(\delta r^2)^{A,114} = r_A^2 - r_{114}^2$ extracted from experimental data [39, 56] and our calculated F_{214} and K_{214} to those determined recently using a CKP method [39]. The radii of odd isotopes and isomers [72] could also be extracted after calculating off-diagonal hyperfine elements. For ^{118,120,122}Cd, measured only using an atomic transition at 509 nm, we use F_{509} and K_{509} given in table 3. Our reported uncertainty is 0.7%–0.9%, dominated by the calculated F_{214} uncertainty, in turn stemming from a systematic uncertainty in the QED correction. For all $(\delta r^2)^{A,114}$, it is smaller than the uncertainty from the CKP method, especially for neutron-rich isotopes, for which the uncertainty can be as much as a factor of four smaller. A slight disagreement is found for mass numbers 112 and lower as seen in figure 4(a), which we ascribe to the limitations the CKP method listed above. Our improved charge radii increase the disagreement with state-of-the-art nuclear theory calculations [39, 56] for the most neutron rich isotopes (figure 4(b)), while improving the agreement for those that are proton-rich (figure 4(a)).

The benefit of extracting radii directly from calculated atomic constants is even more pronounced for the ladder differences $(\delta r^2)^{A+2,A} = r_{A+2}^2 - r_A^2$, which are highly sensitive to the uncertainties of muonic x-ray measurements. Such differences are useful, e.g. for identifying quantum phase transitions in nuclear shapes [73, 74]. Our results in table 4 are up to 60 times more accurate than those obtained with a CKP method [71].

Table 4. Updated differences of charge radii of even–even Cd isotopes in fm^2. This work and [39] use measurements for the D2 line from [39, 56], while the radii extracted using atomic factors from the MCDHF method [64] utilize measurements in the intercombination line summarized in [71]. The charge radius is obtained by adding $(r_c)^{114} = 4.614(3)$ fm in quadrature.

A	$(\delta r^2)^{A,114}$	CKP [39]	MCDHF [64]	$(\delta r^2)^{A+2,A}$	[71]
100	−1.466(12)	−1.409(19)	—	0.2876(23)	—
102	−1.178(9)	−1.135(14)	—	0.2480(20)	0.28(12)
104	−0.930(8)	−0.897(10)	—	0.2149(18)	0.235(95)
106	−0.714(6)	−0.690(8)	−0.662(24)	0.1899(15)	0.182(16)
108	−0.524(4)	−0.506(6)	−0.478(19)	0.1817(15)	0.183(15)
110	−0.343(3)	−0.331(4)	−0.310(12)	0.1791(14)	0.174(13)
112	−0.164(1)	−0.158(2)	−0.145(6)	0.1635(13)	0.157(10)
114	0	0	0	0.1360(11)	0.129(10)
116	0.136(1)	0.134(2)	0.115(5)	0.1108(27)	0.083(22)
118	0.248(2)	0.244(6)	—	0.1003(25)	0.084(50)
120	0.349(3)	0.344(8)	—	0.0892(19)	—
122	0.439(4)	0.434(11)	—	0.0825(31)	—
124	0.520(5)	0.514(14)	—	0.0760(9)	—
126	0.596(5)	0.590(18)	—	0.0755(9)	—
128	0.671(6)	0.666(21)	—	0.0443(8)	—
130	0.716(7)	0.713(24)	—	—	—

Figure 4. Squared RMS charge radii of even–even Cd isotopes relative to ^{114}Cd. (a): proton rich, (b): neutron rich. The data points correspond to columns 2–4 of table 4. The nuclear theory lines are from the Fayans functional (Fy), extended by information on the radii of Ca [56], and Skyrme–Hartree–Fock–Bogoliubov mass formula (HFB-24) [39].

8. Towards BSM physics

We can use the above results to assess the requirements for KPs in Cd I ISs to be sensitive to new physics. An interaction between electrons and neutrons that is mediated by a heavy boson has a short range, less than a Bohr radius. To leading order, it is a contact interaction, proportional to the wave function overlap with the nucleus, and therefore proportional to the FS. Such a contribution is absorbed into charge radii differences, so it does not create deviations of linearity in KPs. In the next order, and in a hydrogenic approximation, the deviation from linearity turns out to be roughly proportional to the FS [8]. Therefore, a KP for transitions i and j where $|F_i - F_j|$ is large, can have a high sensitivity to such new physics. In figure 1(b) we plot $|F_i - F_j|$ for important transition pairs, whose atomic constants are given in table 3. As expected, large differences are between pairs that do not share the same S state. However, narrow transitions couple the ground S state with the $5p\,^3P_j$ states, enabling exceptional precisions for their measurements. Focusing on the clock and intercombination line pair, a KP returns $F_{332,326} = 1.008(13)$, with an uncertainty largely from the 468 nm measurement [55] and our 480 nm measurement. Multiplying by $F_{326} = -4354(62)$ MHz fm^{-2} from table 3, we find $|F_{332} - F_{326}| \leqslant 100$ MHz fm^{-2}. For the $S - D$ transitions used in the KP of Ca II, $|F_{732} - F_{729}| = 0.55(2)$ MHz fm^{-2} [13], which is up to two orders of magnitude smaller. We therefore surmise that when searching for new interactions mediated by a heavy boson, the sensitivity of a KP between the ISs of the clock and intercombination lines in Cd could be as much as two orders more sensitive than the current limit set by IS measurements in Ca II. As the accuracy of measurements in the latter are of order

20 Hz, accuracies of at least few kHz would be required for Cd I. Considering that the natural linewidth of the intercombination line is 69 kHz, such an accuracy should be straightforward with trapped samples.

It is difficult to attribute an observed KP non-linearity to new physics without estimating non-linear SM contributions, such as the quadratic mass shift (QMS). Due to the similarity between nuclear masses and mass numbers, the deviation pattern of the QMS is nearly indistinguishable from the pattern induced by a new boson that couples electrons and neutrons, and so it sets a stringent limit on the new physics reach. The order of magnitude of the QMS can be estimated with a hydrogenic approximation to be $K_{ij}^{\mathrm{QMS}} = K_{ij}(m/M_A + m/M_{A'})$ [75], with $|K_{332,326}^{\mathrm{QMS}}| \leqslant 60$ GHz u from our KP. A linear fit of $K_{332,326}^{\mathrm{QMS}}$ versus $\delta\bar{\nu}_{326}^{A,A+2}$ returns an offset of 0.7 MHz u, a slope of 6×10^{-10}, and, most importantly, isotope-dependent non-linearities. The largest deviation from the linear fit is 4 Hz, for the ^{106,108}Cd pair and the maximum value of $K_{332,326}$. It is comparable to the estimated 3 Hz QMS-induced non-linearity in Ca II [76].

For the medium mass Cd system, with its small nuclear deformations, the largest expected SM non-linearity is the quadratic field shift (QFS) [15]. In the notation of equation (8), it takes the form $F_{ij}^{\mathrm{QFS}} = G_{ij}(\delta(r^2)^{AA'})^2/\mu_{AA'}$, where $G_{ij} = G_i - F_{ij}G_j$. G_{ij} sets the scale of the non-linearity and is a transition-dependent and nucleus-independent constant [16, 17]. This scale is difficult to estimate and different calculations yield a wide range of sensitivities [16]. Assuming that the QFS is approximately quadratic in $|F_i - F_j|$, the absence of observed KP non-linearities in this work already indicates that the non-linearity induced by the QFS of the narrow transition pairs is less than 1 kHz. Moreover, the QFS may be identified from the deviation pattern from linearity [17]. The precisions with which $\delta(r^2)$ are known set the limits for this identification, thus emphasizing the need for the improved radii in table 4.

Other sources of non-linearity, such as nuclear polarization and nuclear deformation, could be non-negligible at the anticipated level of precision [15, 77, 78]. Calculating their magnitude and pattern is difficult due to our limited understanding of nuclear structure. However, like the QFS, their magnitude increases with the wave function overlap with the nucleus. By combining the ISs of three or more transitions with different FSs, these non-linearities can be isolated [10, 79]. Based on the above considerations, the ISs of the clock and intercombination lines can be measured to the order of $\sim$100 Hz, limited by the natural linewidth of the intercombination line. If no non-linearity is observed, the ultra-narrow 314 nm line may provide higher precision with reasonably controlled tensor light shift. If a non-linearity is present at this level, the IS of a transition that does not include the ground state can lead to a sensitive multi-dimensional KP. As suggested by figure 1(b), the $|F_i - F_j|$ for these transitions are at least two orders of magnitude larger than for ground state transitions. Narrow transitions between excited states, such as from $^3P_0$ to long-lived low-lying Rydberg states, can thus increase the sensitivity of searches for BSM physics.

9. Summary

The measurements reported here significantly improve the ISs of several low-lying transitions of Cd I, including the first measurements of two transitions. For the wide 229 nm and the narrow 326 nm transitions, we utilize a cryogenic beam with enriched samples, combined with a detection method that distinguishes between the emission patterns of bosonic and fermionic isotopes. We also measured ISs of the 326 and 361 nm transitions using the sharp blue edge of laser-cooling in a magneto-optical trap, and of the 480 nm transition via optical pumping of the trapped atoms. Combining our 480 and 326 nm ISs with previous ISs for the 486 [55] and 509 nm [56] transitions, we predict the ISs of the two ultra-narrow transitions in Cd, which have not yet been measured. Our results are significantly more accurate, often in disagreement with previous measurements, and highlight the benefits of isotope-selective and cold sources for IS measurements.

We also present high-precision calculations of IS constants of Cd II. By projecting our calculations from Cd II to Cd I, using KPs with measured ISs, we find the IS constants for all low-lying transitions in Cd I, including those of the narrow intercombination and ultra-narrow lines. Our resulting IS constants largely agree with, and are more accurate than those obtained from the CI-MBPT [39] and MCDHF methods [64], setting stringent benchmarks for improving the theory. Some disagreements are observed with recent calculations [64], potentially from underestimating the uncertainty of high-order electron correlations as well as the importance of the QED contributions to the field shift constants.

By combining our calculated IS constants with measurements of a long chain of short-lived ions, we extract accurate charge radii differences, without the limitations from muonic atom measurements. To our knowledge, this is the first extraction of charge radii differences for a chain of isotopes with an accuracy better than 1%, which opens opportunities to improve our knowledge of nuclear sizes far from stability. Beyond benchmarking nuclear models, these are important to identify the patterns of non-linearities in future high-precision measurements [23]. This work sets the stage for new physics searches using generalized

KPs in the Cd system. Our results suggest that precise future Cd IS measurements can improve, by as much as two orders of magnitude, the current best bounds on new electron–neutron interactions, obtained from a KP for Ca II transitions.

Data availability statement

The data that support the findings of this study are available upon reasonable request from the authors.

Acknowledgments

ORCID iDs

B Ohayon https://orcid.org/0000-0003-0045-5534
S Hofsäss https://orcid.org/0000-0001-6805-7044
S Truppe https://orcid.org/0000-0002-0121-6538
B K Sahoo https://orcid.org/0000-0003-4397-7965

References

[1] BACON Collaboration 2021 Frequency ratio measurements at 18-digit accuracy using an optical clock network *Nature* **591** 564
[2] Derevianko A and Pospelov M 2014 Hunting for topological dark matter with atomic clocks *Nat. Phys.* **10** 933
[3] Safronova M S, Budker D, DeMille D, Kimball D F J, Derevianko A and Clark C W 2018 Search for new physics with atoms and molecules *Rev. Mod. Phys.* **90** 025008
[4] Takamoto M, Ushijima I, Ohmae N, Yahagi T, Kokado K, Shinkai H and Katori H 2020 Test of general relativity by a pair of transportable optical lattice clocks *Nat. Photon.* **14** 411
[5] Lange R, Huntemann N, Rahm J M, Sanner C, Shao H, Lipphardt B, Tamm C, Weyers S and Peik E 2021 Improved limits for violations of local position invariance from atomic clock comparisons *Phys. Rev. Lett.* **126** 011102
[6] King W H 1963 Comments on the article "Peculiarities of the isotope shift in the samarium spectrum" *J. Opt. Soc. Am.* **53** 638
[7] Delaunay C, Ozeri R, Perez G and Soreq Y 2017 Probing atomic Higgs-like forces at the precision frontier *Phys. Rev.* D **96** 093001
[8] Berengut J C *et al* 2018 Probing new long-range interactions by isotope shift spectroscopy *Phys. Rev. Lett.* **120** 091801
[9] Stadnik Y V 2018 Probing long-range neutrino-mediated forces with atomic and nuclear spectroscopy *Phys. Rev. Lett.* **120** 223202
[10] Berengut J C, Delaunay C, Geddes A and Soreq Y 2020 Generalized King linearity and new physics searches with isotope shifts *Phys. Rev. Res.* **2** 043444
[11] Manovitz T, Shaniv R, Shapira Y, Ozeri R and Akerman N 2019 Precision measurement of atomic isotope shifts using a two-isotope entangled state *Phys. Rev. Lett.* **123** 203001
[12] Zheng X, Dolde J, Lochab V, Merriman B N, Li H and Kolkowitz S 2022 Differential clock comparisons with a multiplexed optical lattice clock *Nature* **602** 425
[13] Solaro C, Meyer S, Fisher K, Berengut J C, Fuchs E and Drewsen M 2020 Improved isotope-shift-based bounds on bosons beyond the standard model through measurements of the $^2D_{3/2} - ^2D_{5/2}$ interval in Ca$^+$ *Phys. Rev. Lett.* **125** 123003
[14] Drake G W F, Dhindsa H S and Marton V J 2021 King and second-King plots with optimized sensitivity for lithium ions *Phys. Rev.* A **104** L060801
[15] Munro-Laylim P, Dzuba V A and Flambaum V V 2021 Nuclear polarisation and relativistic effects contributions to King plot non-linearity (arXiv:2112.14313 [physics.atom-ph])
[16] Counts I, Hur J, Aude Craik D P L, Jeon H, Leung C, Berengut J C, Geddes A, Kawasaki A, Jhe W and Vuletić V 2020 Evidence for nonlinear isotope shift in Yb$^+$ search for new Boson *Phys. Rev. Lett.* **125** 123002
[17] Ono K, Saito Y, Ishiyama T, Higomoto T, Takano T, Takasu Y, Yamamoto Y, Tanaka M and Takahashi Y 2022 Observation of nonlinearity of generalized King plot in the search for new Boson *Phys. Rev.* X **12** 021033
[18] Figueroa N L, Berengut J C, Dzuba V A, Flambaum V V, Budker D and Antypas D 2022 Precision determination of isotope shifts in ytterbium and implications for new physics *Phys. Rev. Lett.* **128** 073001
[19] Hur J *et al* 2022 Evidence of two-source King plot nonlinearity in spectroscopic search for new Boson *Phys. Rev. Lett.* **128** 163201
[20] Ebata S and Nakatsukasa T 2017 Octupole deformation in the nuclear chart based on the 3D Skyrme Hartree–Fock plus BCS model *Phys. Scr.* **92** 064005
[21] Schussheim D and Gibble K 2018 Laser system to laser-cool and trap cadmium: towards a cadmium optical lattice clock *Frontiers in Optics/Laser Science* (Optical Society of America) p LTh1F.2
[22] Yamaguchi A, Safronova M S, Gibble K and Katori H 2019 Narrow-line cooling and determination of the magic wavelength of Cd *Phys. Rev. Lett.* **123** 113201
[23] Müller R A, Yerokhin V A, Artemyev A N and Surzhykov A 2021 Nonlinearities of King's plot and their dependence on nuclear radii *Phys. Rev.* A **104** L020802
[24] King W H 2013 *Isotope Shifts in Atomic Spectra* (New York: Springer) (https://doi.org/10.1007/978-1-4899-1786-7)
[25] Blundell S A, Baird P E G, Palmer C W P, Stacey D N and Woodgate G K 1987 A reformulation of the theory of field isotope shift in atoms *J. Phys. B: At. Mol. Phys.* **20** 3663

[26] Gillespie W A, Brain S W, Johnston A, Lees E W, Singhal R P, Slight A G, Brimicombe M W S M, Stacey D N, Stacey V and Huhnernann H 1975 Measurements of the nuclear charge distribution in the cadmium isotopes *J. Phys. G: Nucl. Phys.* **1** L6

[27] Lightbody J W, Penner S, Fivozinsky S P, Hallowell P L and Crannell H 1976 Electron scattering from vibrational nuclei *Phys. Rev. C* **14** 952

[28] Palmer C W P 1987 Reformulation of the theory of the mass shift *J. Phys. B: At. Mol. Phys.* **20** 5987

[29] Shabaev V M 1998 QED theory of the nuclear recoil effect in atoms *Phys. Rev. A* **57** 59

[30] Sahoo B K and Ohayon B 2021 Benchmarking many-body approaches for the determination of isotope-shift constants: application to the Li, Be$^+$ and Ar^{15+} isoelectronic systems *Phys. Rev. A* **103** 052802

[31] Estévez G and Bhuiyan L B 1985 Electrostatic potential due to a Fermi-type charge distribution *Am. J. Phys.* **53** 450

[32] Lindgren I and Morrison J 1982 *Atomic Many-Body Theory* vol 13 (Berlin: Springer)

[33] Mukhopadhyay D and Mukherjee D 1989 Size-extensive effective Hamiltonian formalisms using quasi-Hilbert and quasi-Fock space strategies with incomplete model spaces *Chem. Phys. Lett.* **163** 171

[34] Sahoo B K, Majumder S, Chaudhuri R K, Das B P and Mukherjee D 2004 *Ab initio* determination of the lifetime of the $6^2P_{3/2}$ state for ^{207}Pb$^+$ by relativistic many-body theory *J. Phys. B: At. Mol. Opt. Phys.* **37** 3409

[35] Sahoo B K *et al* 2020 Analytic response relativistic coupled-cluster theory: the first application to indium isotope shifts *New J. Phys.* **22** 012001

[36] Boys S F and Lennard-Jones J E 1951 Electronic wave functions III. Some theorems on integrals of antisymmetric functions of equivalent orbital form *Proc. R. Soc.* A **206** 489

[37] Shenstone A G and Pittenger J T 1949 Cadmium spectra *J. Opt. Soc. Am.* **39** 219

[38] Burns K and Adams K B 1956 Energy levels and wavelengths of natural cadmium and of cadmium-114 *J. Opt. Soc. Am.* **46** 94

[39] Han J Z *et al* 2022 Isotope shift factors for the Cd$^+$ $5s^2S_{1/2} \rightarrow 5p^2P_{3/2}$ transition and determination of Cd nuclear charge radii *Phys. Rev. Res.* **4** 033049

[40] Ohayon B, Ruiz R F G, Sun Z H, Hagen G, Papenbrock T and Sahoo B K 2022 Nuclear charge radii of Na isotopes: interplay of atomic and nuclear theory *Phys. Rev. C* **105** L031305

[41] Finkelstein B 1928 Über den Virialsatz in der Wellenmechanik *Z. Phys.* **50** 293

[42] Li J, Nazé C, Godefroid M, Gaigalas G and Jönsson P 2012 On the breakdown of the Dirac kinetic energy operator for estimating normal mass shifts *Eur. Phys. J. D* **66** 1

[43] Lindroth E and Mårtensson-Pendrill A-M 1983 Calculation of the isotope shift in Na *Z. Phys.* A **309** 277

[44] Heylen H *et al* 2016 Changes in nuclear structure along the Mn isotopic chain studied via charge radii *Phys. Rev. C* **94** 054321

[45] Heylen H *et al* 2021 High-resolution laser spectroscopy of $^{27-32}$Al *Phys. Rev. C* **103** 014318

[46] Koszorús A *et al* 2021 Charge radii of exotic potassium isotopes challenge nuclear theory and the magic character of N = 32 *Nat. Phys.* **17** 439

[47] Dzuba V A, Johnson W R and Safronova M S 2005 Calculation of isotope shifts for cesium and francium *Phys. Rev. A* **72** 022503

[48] Shi C *et al* 2018 Unexpectedly large difference of the electron density at the nucleus in the $4p^2$ P$_{1/2,3/2}$ fine-structure doublet of Ca$^+$ *Exploring the World With the Laser* (Berlin: Springer) pp 1–19

[49] Safronova M S and Johnson W R 2001 Third-order isotope-shift constants for alkali-metal atoms and ions *Phys. Rev. A* **64** 052501

[50] Tupitsyn I I, Shabaev V M, Crespo López-Urrutia J R, Draganić I, Soria Orts R and Ullrich J 2003 Relativistic calculations of isotope shifts in highly charged ions *Phys. Rev. A* **68** 022511

[51] Berengut J C, Dzuba V A and Flambaum V V 2003 Isotope-shift calculations for atoms with one valence electron *Phys. Rev. A* **68** 022502

[52] Dorne A, Sahoo B K and Kastberg A 2021 Relativistic coupled-cluster calculations of isotope shifts for the low-lying states of Ca II in the finite-field approach *Atoms* **9** 26

[53] Schelfhout J S and McFerran J J 2021 Isotope shifts for $^1S_0 - ^3P^o_{0,1}$ Yb lines from multiconfiguration Dirac-Hartree-Fock calculations *Phys. Rev. A* **104** 022806

[54] Hofsäss S, Padilla-Castillo J E, Wright S C, Kray S, Thomas R, Sartakov B G, Ohayon B, Meijer G and Truppe S 2022 High-resolution isotope-shift spectroscopy of Cd I (arXiv:2210.11425)

[55] Wenz R, Timmermann A and Matthias E 1981 Subshell effect in mean square charge radii of stable even cadmium isotopes *Z. Phys.* A **303** 87

[56] Hammen M *et al* 2018 From calcium to cadmium: testing the pairing functional through charge radii measurements of $^{100-130}$Cd *Phys. Rev. Lett.* **121** 102501

[57] Tinsley J N, Bandarupally S, Penttinen J-P, Manzoor S, Ranta S, Salvi L, Guina M and Poli N 2021 Watt-level blue light for precision spectroscopy, laser cooling and trapping of strontium and cadmium atoms *Opt. Express* **29** 25462

[58] Kelly F M and Tomchuk E 1959 Isotope shift in the CdI intercombination resonance line λ 3261 Å *Proc. Phys. Soc.* **74** 689

[59] Kloch R, Baird P, Boshier M, Macpherson M, Palmer C, Stacey D and Stacey V 1987 Isotope shifts in λ 326.1 nm of CdI *Z. Phys.* D **6** 315

[60] Kelly F M and Tomchuk E 1961 Isotope shift in the CdI resonance line 2288 *Proc. Phys. Soc.* **78** 1304

[61] Brix P and Steudel A 1950 Die isotopieverschiebung in der Cd I-Resonanzlinie λ 3261 Å *Z. Phys.* **128** 260

[62] Leś F 1964 *Acta Phys. Pol.* **24** 951

[63] Buchinger F, Dabkiewicz P, Kluge H-J, Mueller A and Otten E-W 1987 The n-dependence of Cd mean square charge radii (54 ⩽ N ⩽ 72) and the nuclear moments of ^{103}Cd *Nucl. Phys.* A **462** 305

[64] Schelfhout J S and McFerran J J 2022 Multiconfiguration Dirac-Hartree-Fock calculations for Hg and Cd with estimates for unknown clock-transition frequencies *Phys. Rev. A* **105** 022805

[65] Ting Y and Lew H 1957 Hyperfine structure of Cu^{6}3 and Cu^{6}5 *Phys. Rev.* **105** 581

[66] Walhout M, Megens H J L, Witte A and Rolston S L 1993 Magneto-optical trapping of metastable xenon: isotope-shift measurements *Phys. Rev. A* **48** R879

[67] Bodermann B, Knöckel H and Tiemann E 2002 Widely usable interpolation formulae for hyperfine splittings in the ^{127}I$_2$ spectrum *Eur. Phys. J. D* **19** 31

[68] Contreras R and Kelly F 1969 Isotope shift in the second spectrum of cadmium *Can. J. Phys.* **47** 1979

[69] Bishop D C and King W H 1971 Isotope shifts in the resonance lines of Cd II and Sn IV and the size of specific mass shifts in alkali like resonance lines *J. Phys. B: At. Mol. Phys.* **4** 1798

[70] Brimicombe M, Stacey D, Stacey V, Hühnermann H and Menzel N 1976 Optical isotope shifts and hyperfine structure in Cd *Proc. R. Soc.* A **352** 141

[71] Fricke G and Heilig K 2004 *Nuclear Charge Radii · 48-Cd Cadmium* (*Landolt-BÖrnstein—Group I Elementary Particles, Nuclei and Atoms* vol 20) (Berlin: Springer)

[72] Yordanov D T *et al* 2016 Simple nuclear structure in $^{111-129}$Cd from atomic isomer shifts *Phys. Rev. Lett.* **116** 032501

[73] Zerguine S, Van Isacker P and Bouldjedri A 2012 Consistent description of nuclear charge radii and electric monopole transitions *Phys. Rev. C* **85** 034331

[74] Gavrielov N, Leviatan A and Iachello F 2022 Zr isotopes as a region of intertwined quantum phase transitions *Phys. Rev. C* **105** 014305

[75] Yerokhin V A, Müller R A, Surzhykov A, Micke P and Schmidt P O 2020 Nonlinear isotope-shift effects in Be-like, B-like and C-like argon *Phys. Rev. A* **101** 012502

[76] Flambaum V V, Geddes A J and Viatkina A V 2018 Isotope shift, nonlinearity of King plots and the search for new particles *Phys. Rev. A* **97** 032510

[77] Flambaum V V, Samsonov I B, Tan H B T and Viatkina A V 2021 Nuclear polarization effects in atoms and ions *Phys. Rev. A* **103** 032811

[78] Allehabi S O, Dzuba V A, Flambaum V V and Afanasjev A V 2021 Nuclear deformation as a source of the nonlinearity of the King plot in the Yb^{+} ion *Phys. Rev. A* **103** L030801

[79] Frugiuele C, Fuchs E, Perez G and Schlaffer M 2017 Constraining new physics models with isotope shift spectroscopy *Phys. Rev. D* **96** 015011